Fundamental properties of Octalithium Plumbate ceramic breeder material

Andrew W. Davies, Samuel T. Murphy*

Engineering Department, Lancaster University, Bailrigg, Lancaster, LA1 4YW, UK.

Abstract

Octalithium plumbate (Li_8PbO_6) is a candidate for use as a breeder material in future D-T tokamak fusion reactor designs. Key to the development of a breeder blanket is the characterisation of candidate materials. Therefore, density functional theory (DFT) simulations are used to examine the fundamental elastic, electronic and thermal properties of Li_8PbO_6. A comparison is made between two different DFT simulation packages to demonstrate the validity of the results given in this article and as compensation for a lack of experimental data to compare to in the literature. Finally, formation energies are calculated for lithium vacancy defects as well as tritium accommodated as substitutional defects on the lithium site, as these are expected to be some of the most common types of defect in the breeder blanket during reactor operation.

1. Introduction

Nuclear fusion offers the prospect of large quantities of low carbon electricity without generating the long lived radioactive waste associated with today's fission reactors. A future fusion reactor will employ the D-T reaction between two isotopes of hydrogen, deuterium and tritium, i.e.:

$$ {}^{3}_{1}\mathrm{T} + {}^{2}_{1}\mathrm{D} \rightarrow {}^{4}_{2}\mathrm{He} + {}^{1}_{0}n. \quad (1) $$

Reaction 1 releases a large quantity of energy predominantly in the form of kinetic energy of the neutron. Both reactant nuclides occur naturally, however, given its short half-life of 12.6 years tritium only exists in trace quantities primarily in seawater at a concentration of approximately 1 in 10^{18} hydrogen atoms[1], equating to a total inventory of a few kilograms. Such scarcity means there is insufficient tritium to sustain a fleet of fusion reactors. Therefore, maintaining the supply of tritium, often referred to as the tritium economy, is fundamental to the sustainability of fusion energy.

Tritium can be obtained from the transmutation of lithium by high energy neutrons according to:

$$ {}^{7}_{3}\mathrm{Li} + {}^{1}_{0}n \rightarrow {}^{3}_{1}\mathrm{T} + {}^{4}_{2}\mathrm{He} + {}^{1}_{0}n \quad (2) $$

and

$$ {}^{6}_{3}\mathrm{Li} + {}^{1}_{0}n \rightarrow {}^{3}_{1}\mathrm{T} + {}^{4}_{2}\mathrm{He}. \quad (3) $$

A future fusion reactor will be wrapped in a breeder blanket that will contain a lithium based material that will capture the neutrons ejected from the plasma for tritium breeding. The tritium must then be extracted from the blanket for use in the plasma. To ensure that the whole process is sustainable it is essential that at least 1 tritium atom can be recovered from the blanket for every fusion reaction that occurs in the plasma, i.e. the tritium breeding ratio must be greater than unity.

In addition to breeding tritium the blanket region is where the neutron energy is converted into heat for electricity generation while simultaneously providing shielding for the magnets and other ancillary systems. Given the multiple roles for the blanket region, it is perhaps unsurprising, that the choice of breeder material is complicated and inevitably impacts other choices in the construction of a future reactor. There are an array of different breeder blanket concepts that are due to be tested on ITER[2]. In general, these employ either a lithium ceramic or liquid lithium lead eutectic as breeder material.

Ceramic breeder materials are advantageous due to their high lithium densities and their low chemical reactivity[3]. This ensures a degree of safety even in the event of a loss of coolant accident. However, ceramic materials have relatively low thermal conductivities, which will impact the thermal efficiency of the reactor. By contrast the liquid lithium lead concepts offer

*Corresponding Author

Email address: samuel.murphy@lancaster.ac.uk (Samuel T. Murphy)

a higher thermal efficiency[4], however, the reactivity of the liquid metal poses a safety issue, particularly if water is used as a coolant[5]. The liquid breeder concepts also offer an easier refuelling route that may reduce reactor downtime, thereby increasing availability. Ceramic breeder materials currently offer a more near-term solution for effective tritium breeding due to the lack of technological innovation required in comparison with liquid breeder concepts[6].

Of the ceramics breeder materials recent attention has focused on two leading candidates, lithium orthosilicate (Li_4SiO_4) and lithium metatitate (Li_2TiO_3). With some more recent studies looking at developing hybrid ceramic breeder pebbles[7] or creating core shell Li_2TiO_3/Li_4SiO_4 pebbles[8, 9]. Irrespective, it is necessary to enrich with ^{6}Li and to employ a neutron multiplier to achieve the desired TBR. The principle neutron multiplier material is beryllium (typically in $Be_{12}Ti$)[10], however, there is now a desire to reduce the reliance on this element as it is relatively rare and is found to contain traces of uranium. As a consequence, Hernandez and Pereslavtsev re-examined a wide range of solid breeder materials[11]. Of the oxides considered, octalithium plumbate (Li_8PbO_6) was predicted to offer the highest TBR, at least partially due to the Pb which also offers an (*n,2n*) neutron multiplying reaction. Previous experiments have also indicated favourable tritium release characteristics[12]. Palermo *et al.* have proposed a design for a solid breeder blanket based on Li_8PbO_6 via a neutronics assessment which also suggested potential for high tritium release[13]. There are, however, concerns regarding the high temperature stability of the material.

Despite its potential for use as a breeder material in a future fusion reactor, the fundamental properties of Li_8PbO_6 have not been widely studied and there is a requirement to understand more about this material, including basic thermodynamic and elastic data as well as how tritium may be accommodated in the lattice. In recent years there has been a significant growth in the use of atomistic simulation to examine the properties of ceramic breeder materials[14, 15] as well as tritium solubility[16, 17] and diffusivity[18]. Therefore, the present work will use density functional theory (DFT), to calculate key electronic, elastic and thermodynamics properties of Li_8PbO_6 as well as offering a first examination of how tritium may be accommodated in the lattice.

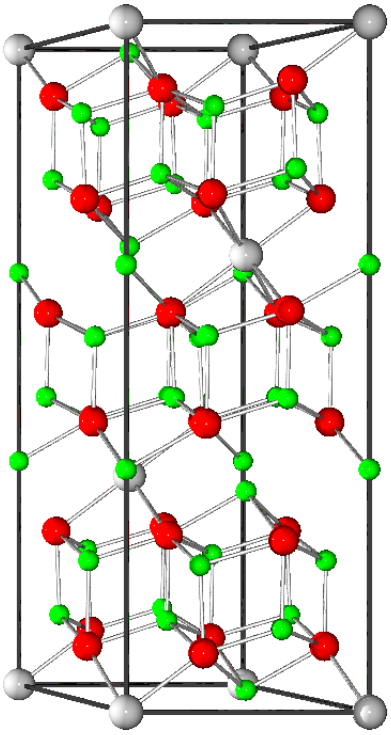

Figure 1: Crystal structure of octalithium plumbate, Li_8PbO_6. Grey, green and red spheres represent the lead, lithium and oxygen ions respectively. The black outline represents the edges of a single unitcell.

2. Crystallography

Li_8PbO_6 crystallises in a trigonal crystal structure that can be described by the $R\bar{3}H$ space group (number 148). Within the unitcell the lead ions occupy the 3a Wyckoff sties and the oxygen ions are all symmetrically equivalent and occupy the 18f positions. By contrast, there are two symmetrically distinct Li positions, the tetrahedrally co-ordinated 18f site and the octahedrally co-ordinated 6c site. As shown in figure 1, Li_8PbO_6 adopts a complex layered structure arranged in sequence -$PbLi_2$-O_3-Li_3-Li_3-O_3- with the Pb in the mixed cation layer displaced by 1/3 in the *x* and *y* directions between each layer. The pure Li layers are composed of the tetrahedrally co-ordinated Li ions and the octahedrally co-ordinated Li occurs only in the mixed cation layer.

3. Methodology

3.1. DFT parameterisation

Simulations presented were performed using a combination of both VASP (version 5.4.4)[19] and CASTEP (version 18.1)[20, 21] planewave pseudopotential codes. Within DFT an infinite crystal is described using supercells and periodic boundary conditions with special point integration over the Brillouin zone. The majority of simulations for both codes employed the generalised gradient approximation (GGA) of Perdew, Burke and Ernzerhof (PBE)[22], however, due to the failure of such semi-local functionals to accurately reproduce band gaps of materials some hybrid simulations employed the hybrid functional of Heyd, Scuseria and Ernzerhof (HSE06)[23]. Integration over the Brillouin zone was performed using a Monkhorst-Pack grid[24] with 6×6×2 k-points in the unitcell, corresponding to a separation between points of $0.0316\times2\pi$ Å^{-1} in the z-axis and $0.0344\times2\pi$ Å^{-1} along the x and y axes. Note that the k-point grid was reduced to a single k-point at Γ for the hybrid simulations in CASTEP due to computational constraints, although it is not anticipated that this will dramatically impact the results. Atoms in CASTEP simulations were represented using norm-conserving pseudopotentials based on the default strings in CASTEP 18.1, whereas VASP simulations employed projector augmented wave (PAW)[25] pseudopotentials. Consequentially, the difference in pseudopotentials used requires different planewave cutoff energies are used to ensure similar convergence. Due to the hardness of the oxygen pseudopotential used in CASTEP a high cutoff energy of 1150 eV was required to ensure a convergence of 0.01 eV per atom. PAW pseudopotentials in VASP allowed the use of a lower cutoff energy of 520 eV to maintain the same level of convergence, although this value was increased by 30% to 650 eV to ensure correct evaluation of the elastic tensor and remained consistent across all calculations. The inclusion of spin-orbit coupling in simulations was not found to have a significant contribution on results. Both codes were able to reproduce the lattice parameters for Li_8PbO_6 and many of its subsystems as illustrated in table 1.

3.2. Defect formalism

At relatively low temperatures, the difference in vibrational contributions to the free energy between perfect and defect supercells can be safely neglected, so we can approximate ΔG_f^i by ΔE_f^i, calculated from the total energies of the perfect and defective cells according to the formalism of Zhang and Northrup[32]. The defect formation energy is then given by:

$$\Delta E_f = E^T_{\text{defect}} - E^T_{\text{perf}} + \sum_\alpha n_\alpha \mu_\alpha + q_i(E_{\text{VBM}} + \varepsilon_f) + dE, \quad (4)$$

where, E^T_{defect} and E^T_{perf} are the DFT total energies of the system with and without the defect, n_α is the number of atoms added/removed of each atomic species α, μ_α is the chemical potential of each species, q_i is the defect charge, E_{VBM} is the valence band maximum taken from the perfect crystal and ε_f is the Fermi energy relative to the valence band maximum, which is taken to be 0 for defect energy calculations. The chemical potential used for lithium in this paper is taken from the lithium metal and for tritium the chemical potential is taken as $\frac{1}{2}$ of the H_2 molecule. Note that by selecting the chemical potential of lithium as that of the metal means that the energy presented here represents an upper bound for the formation energy of a lithium vacancy defect.

dE is a correction factor applied to the formation energies of charged defects to correct for finite size effects arising due to the use of a relatively small simulation supercell. In this work we employ an electrostatic correction of the form:

$$dE = \frac{1}{2} q_i^2 \nu_m^{scr}, \quad (5)$$

where ν_m^{scr} is the screened Madelung constant for the bulk crystal[33]. Given the low atomic numbers for the atoms added or removed to/from the system it is assumed that the potential alignment correction is negligible[34].

Defect simulations employed a supercell constructed from 2×2×1 repetitions of the relaxed hexagonal unitcell, resulting in a supercell containing 180 atoms. To compensate for the increase in the supercell size the k-point grid sampling grid was reduced to 3×3×2 in order to maintain the sampling density. During minimisation of the defect containing supercell the lattice parameters were fixed in order to represent the dilute limit.

4. Results and Discussion

4.1. Electronic properties

The density of states for both models was calculated using both PBE and HSE functionals, due to the tendency for semi-local functionals to underestimate band gaps. A comparison between density of states calculated in VASP and CASTEP are shown below in figure 2.

Table 1: Table showing the lattice parameters for Li_8PbO_6 and it s subsystems compared to experimental values.

System	Property	CASTEP	VASP	Literature value	Reference
Li_8PbO_6	a /Å	5.59	5.58	5.55	[26]
	c /Å	15.83	15.81	15.64	[26]
Li_2O	a /Å	4.62	4.62	4.54	[27]
PbO_2	a /Å	5.07	5.10	4.971	[28]
	b /Å	6.05	6.07	5.95	[28]
	c /Å	5.55	5.58	5.43	[28]
Li	a /Å	3.43	3.46	3.51	[29]
Pb	a /Å	5.02	5.06	4.95	[30]
O_2	r (O-O) /Å	1.24	1.23	1.21	[31]

There is a strong agreement in the structure of the electronic density of states between both simulation packages, with both showing roughly the same increase in bandgap energy between semi-local and hybrid functionals. PBE-measured bandgap energies of 2.05 eV and 1.94 eV and HSE-measured bandgap energies of 3.25 eV and 3.36 eV were measured for CASTEP and VASP softwares respectively.

The dielectric tensor is calculated using Density Functional Perturbation Theory (DFPT) for both VASP[35] and CASTEP[36] simulation codes. The symmetry of the crystal structure illustrated by the unit cell in figure 1 suggests the dielectric constant in the z axis will differ from the values measured in the x and y axes, which are expected to be the same. Static and high frequency dielectric tensors were calculated using both CASTEP (equations 7 & 8) and VASP (equations 9 & 10) simulation packages and are shown below. Both codes are in close agreement with one another, which are in consensus with the expected anisotropic behaviour of the crystal structure.

$$\bar{\epsilon}_0 = \begin{pmatrix} 12.89 & 0 & 0 \\ 0 & 12.89 & 0 \\ 0 & 0 & 13.84 \end{pmatrix} \quad \bar{\epsilon}_\infty = \begin{pmatrix} 3.67 & 0 & 0 \\ 0 & 3.67 & 0 \\ 0 & 0 & 3.93 \end{pmatrix} \tag{7, 8}$$

$$\bar{\epsilon}_0 = \begin{pmatrix} 13.09 & 0 & 0 \\ 0 & 13.09 & 0 \\ 0 & 0 & 14.29 \end{pmatrix} \quad \bar{\epsilon}_\infty = \begin{pmatrix} 3.96 & 0 & 0 \\ 0 & 3.96 & 0 \\ 0 & 0 & 4.25 \end{pmatrix} \tag{9, 10}$$

The dielectric tensor for Li_8PbO_6 is comparatively low in comparison to other proposed ceramic breeder materials such as Li_2TiO_3[33], which may have a significant impact on ionic conductivity and the mobility of tritium ions in the crystal.

4.2. Elastic properties

The elastic tensor is derived from the stress-strain relationship predicted by performing finite distortions on the crystal in both codes. The elastic response of Li_8PbO_6 is summarised in the elastic constant tensor shown in Table 2. According to Neumann's rules there are seven unique elastic constants for the $R\bar{3}H$ space group, these are c_{11}, c_{12}, c_{13}, c_{14}, c_{15}, c_{33} and c_{44}. Seven more elastic constants can be derived from equivalences with these values, these are: $c_{22} = c_{11}$, $c_{23} = c_{13}$, $c_{24} = -c_{56} = c_{14}$, $c_{25} = c_{64} = -c_{15}$ and $c_{55} = c_{44}$. The final elastic constant is related to these unique elastic constants according to $c_{66} = (c_{11} - c_{12})/2$. It is clear from the data presented that this relation holds for Li_8PbO_6.

Elastic constants were calculated using a 6×6×2 k-point grid on the relaxed hexagonal unit cell. Despite general agreement between codes, there is a slight discrepancy between the c_{11} elastic constants.

The inconsistency in c_{11} manifests in the Young's modulus. Due to the large contribution the c_{11} elastic constant plays particularly in the x and y directions, large differences in c_{11} values between codes can produce radically different values for the Young's moduli. The CASTEP code predicts the x and y components of the Young's modulus is is over 25% greater in comparison with the VASP code. This consequentially equates to CASTEP suggesting Li_8PbO_6 is stiffer in the x and y directions compared with z, in contrast to VASP which suggests the opposite.

4.3. Thermodynamics properties

Due to the scarcity of literature on the physical characteristics of Li_8PbO_6, thermodynamic properties of Li_8PbO_6 were examined in VASP using the Density

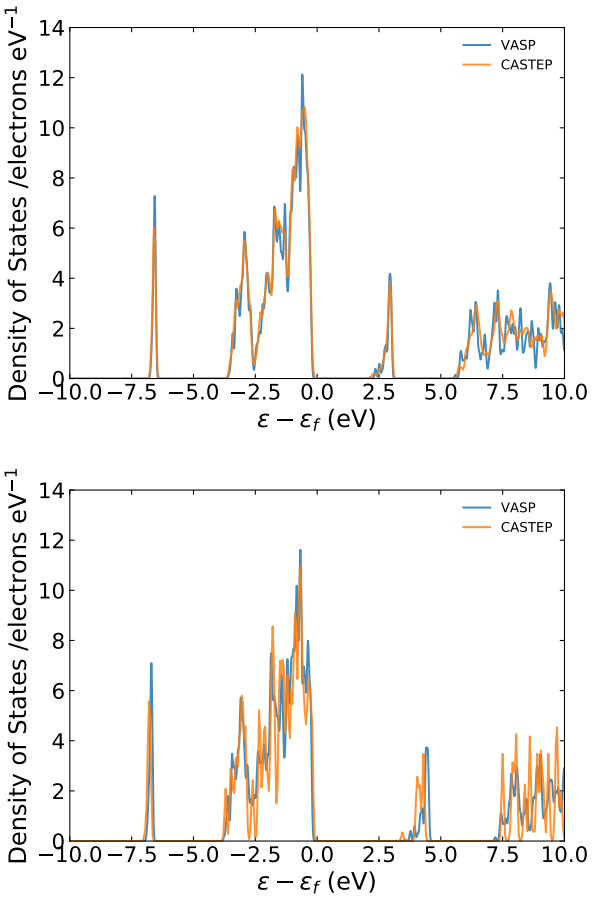

Figure 2: Electronic density of states for Li_8PbO_6 using the PBE and HSE exchange-correlation functionals. Top = PBE, bottom = HSE

Functional Perturbation Theory (DFPT) software package Phonopy[37] and using default phonon calculations provided by CASTEP[38]. As ceramic breeder materials are expected to transfer heat to the reactor coolant and maintain performance in high temperature regimes (>800°C), an understanding of the thermal properties is critical for determining the efficacy of Li_8PbO_6 as a breeder blanket. Phonon density of states for both simulation packages are included in figure 3.

As there is no published value in the literature for the enthalpy of formation of Li_8PbO_6 from Li_2O and PbO_2, Born-Haber cycles were created to demonstrate enthalpies of fomation of the Li_8PbO_6 compound from its constituent elements. There is general agreement in enthalpies of formation between simulation packages. Given that the formation energies of Li_2O and PbO_2 are in reasonable agreement with the literature, the enthalpy of formation of Li_8PbO_6 calculated is likely a reasonable approximation to the true value.

Table 2: Table showing the elastic constants for Li_8PbO_6.

Parameter	CASTEP (GPa)	VASP (GPa)
c_{11}	191.54	163.54
c_{12}	54.27	55.32
c_{13}	53.80	50.11
c_{14}	20.74	21.87
c_{15}	-1.10	-1.98
c_{33}	150.90	161.56
c_{44}	64.50	54.46
c_{66}	68.64	52.63
Bulk modulus	94.74	88.46
Shear modulus	61.61	51.11
Young's Modulus		
x	155.14	121.85
y	155.14	120.03
z	127.34	138.74

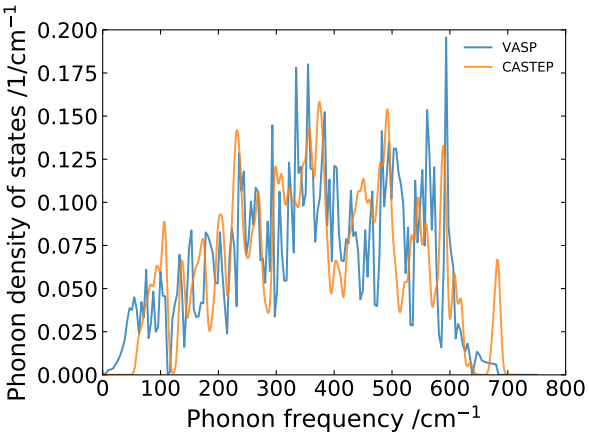

Figure 3: Phonon density of states for Li_8PbO_6.

The relationship between the Helmholtz free energies, internal energy and entropy have been calculated from the phonon density of states. There is very strong agreement between simulation packages as might be expected from the close agreement with the phonon density of states. The internal energy shown in figure 5 becomes roughly linear above approximately 500K. The contribution given by the entropy of the crystal plays a major role in the final result for Helmholtz free energy at high temperatures.

The specific heat for a constant volume C_V has also

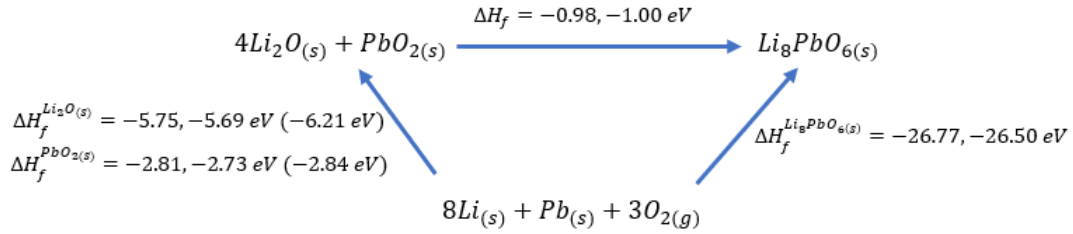

Figure 4: Born-Haber cycle for Li_8PbO_6 and its constituents. First value = VASP, second = CASTEP and bracketed values are obtained from literature[39].

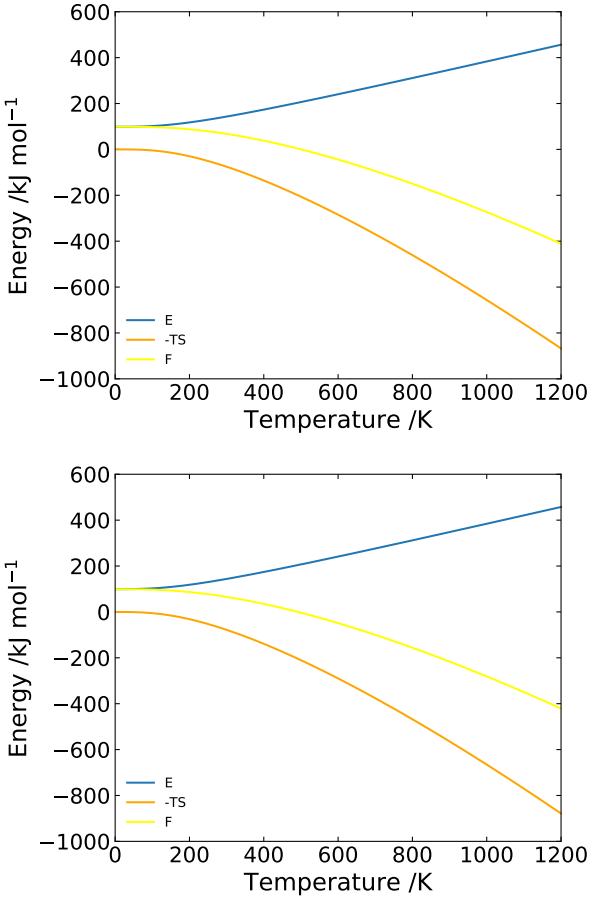

Figure 5: Helmholtz free energy, phonon contributions to internal energy and entropy as a function of temperature for Li_8PbO_6. Top = CASTEP, bottom = VASP

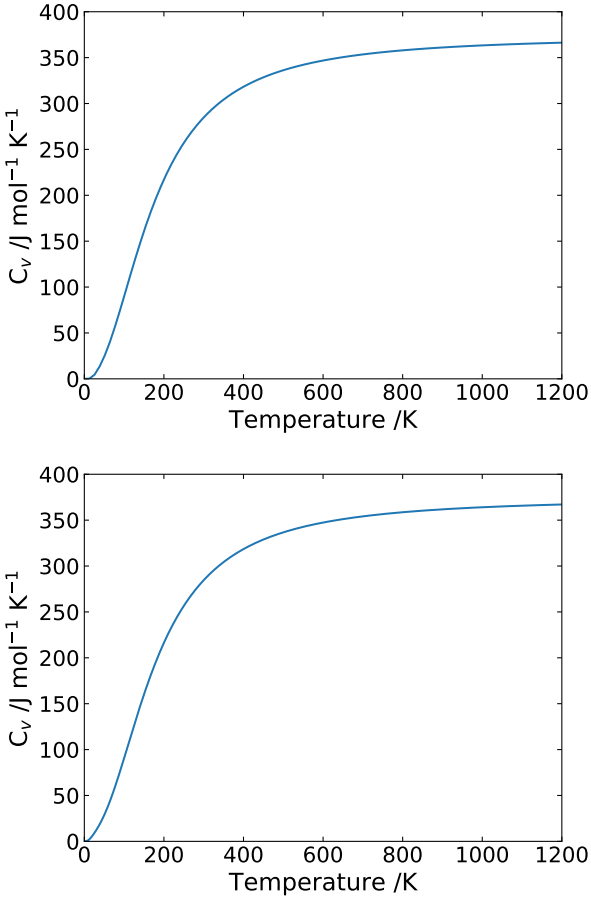

Figure 6: Specific heat for constant volume of Li_8PbO_6 as a function of temperature. Top = CASTEP, bottom = VASP

been calculated and is illustrated in figure 6. An understanding of the specific heat for Li_8PbO_6 is important as ceramic breeder materials are often used dually as a means to transfer heat to the reactor coolant to generate power, due to their close proximity to the fusion plasma. The predicted specific heat of Li_8PbO_6 is generally lower than estimates for other lithium-ceramics, such as the DFT-calculated estimate made by Wan *et al.* for β-Li_2TiO_3[40] and that of Yan *et al.* for Li_4TiO_4[41],

indicating Li_8PbO_6 may be more susceptible to a faster rise in temperature during reactor operation compared to other proposed breeder blanket materials. Although this is not always true as comparisons with other materials such as Li_2SiO_3 [42] predicted by Ma *et al.* are much more promising, with a heat capacity more than twice as high.

4.4. High Temperature Stability

The stability of Li_8PbO_6 at high temperatures has been examined by implementing the quasi-harmonic approximation given by the DFPT package Phonopy to introduce a volume dependence onto the thermal properties of Li_8PbO_6, as well as its constituents. The specific heat for constant pressure C_P, volume-dependent enthalpies and Gibbs free energies were calculated for Li_8PbO_6, Li_2O, PbO_2 and Li_4PbO_4 (sharing the same energy cut-off and k-point density), as traces of Li_4PbO_4 were found to be present during the sintering process for temperatures of 600-800°C, although no traces were found at 1000°C over a period of 24 hours [43]. Therefore, the key processes to consider are:

$$Li_4PbO_4 + 2Li_2O \rightarrow Li_8PbO_6 \quad (10)$$

$$PbO_2 + 4Li_2O \rightarrow Li_8PbO_6 \quad (11)$$

$$PbO_2 + 2Li_2O \rightarrow Li_4PbO_4 \quad (12)$$

Due to the similarity in results for thermodynamic properties between simulation packages, results for this section were produced using only the VASP software. Volumes in the range of ±15% of the relaxed crystal were used in steps of 3% for all materials examined. The resulting heat capacities are presented in figure 7.

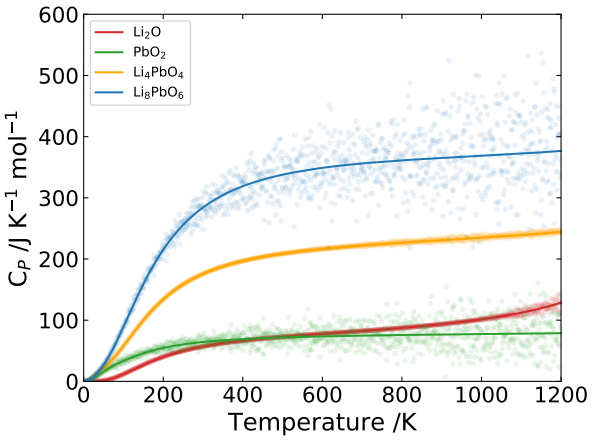

Figure 7: Specific heat for constant pressure of Li_8PbO_6 and its constituents as a function of temperature.

Using these specific heats, it is possible to determine the enthalpy changes associated with reactions 10 - 12, these are illustrated in figure 8. Figure 8 shows that the enhalpy changes are negative across the temperature range, implying the Li_8PbO_6 is the more favourable state and only grows more favourable with increasing temperature. The enthalpy of formation of the reaction $PbO_2 + 2Li_2O \rightarrow Li_4PbO_4$ was also found to be negative, although with a marginal preference towards the formation of Li_8PbO_6 over Li_4PbO_4 and this preference increasing with temperature.

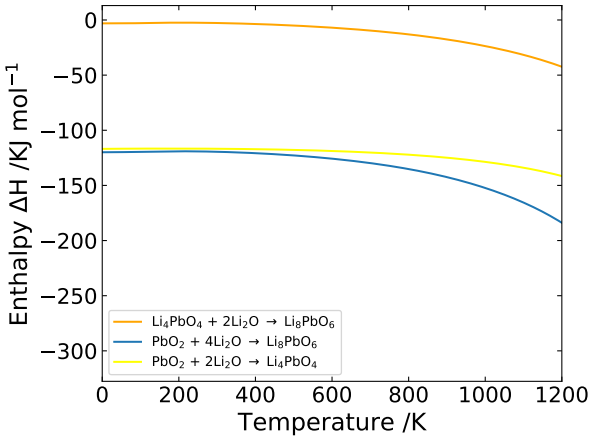

Figure 8: Enthalpy of formation of Li_8PbO_6 and its constituents as a function of temperature.

Examination of the Gibbs formation energy is critical in discussion of the phase stability of Li_8PbO_6. The Gibbs formation energy of Li_8PbO_6 and Li_4PbO_4 from PbO_2 and Li_2O are strongly negative and thus spontaneous. Due to the greater negativity of the entropy in the formation of Li_8PbO_6 compared to Li_4PbO_4, the Gibbs formation energy rises above that of the formation of Li_4PbO_4 at roughly 1000 K. Implying that the Li_8PbO_6 phase is unstable at higher temperatures. Despite the phase instability at high temperatures, Li_8PbO_6 may have some utility in cooler regions of the blanket.

4.5. Lithium vacancy defects

During operation the ceramic breeder material ages and the lithium will be burnt-up to produce tritium resulting in a reduction in its availability in the matrix. This paucity of lithium will be accommodated by point defects such as interstitials and vacancies. As discussed for other ceramic breeder materials it is anticipated that the lithium vacancy defects will play a significant role in the accommodation of this substochiometry[16]. Therefore, the formation energy for the formally charged,

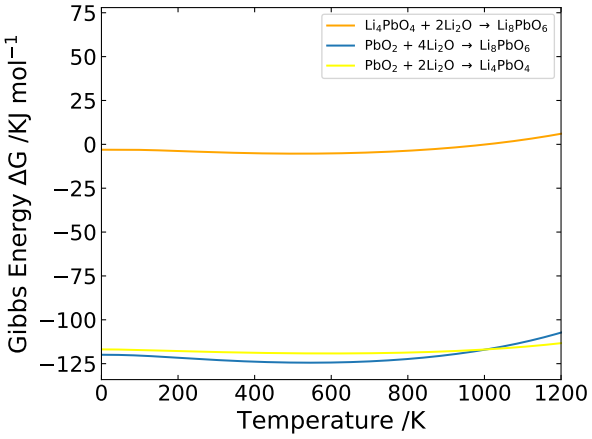

Figure 9: Gibbs formation energy of Li_8PbO_6 and its constituents as a function of temperature.

V_{Li}^{1-}, is examined here and other defects and charge states will be the focus of future work.

As discussed in the Crystallography section there are two symmetrically distinct lithium sites in Li_8PbO_6, therefore the defect formation energy for the two different sites has been calculated and the energies presented in table 3.

Table 3: Defect formation energies for the lithium vacancy defects in Li_8PbO_6.

Lithium site	Wychoff notation	CASTEP E_f /eV	VASP E_f /eV
Li1	18f	3.728	3.641
Li2	6c	4.071	4.007

The data presented in table 3 shows that the formation energy for the vacancy on the tetrahedrally coordinated 18f site is lower than on the octahedrally coordinated 6c site. This implies that the majority of such defects will occur on the 18c Li1 site. Defect formation energies between codes show remarkable agreement with a deviation of less than 0.1 eV between each other for both lithium sites, with VASP measurements being slightly lower. The difference between the two vacancy defects is similar between DFT simulation packages, with values of 0.34 eV and 0.37 eV for CASTEP and VASP respectively. This is larger than the difference between possible Li sites in Li_2TiO_3[14] although significantly smaller than predicted for Li_4SiO_4[44]. In Li_8PbO_6, the origin of this discrepancy is the increased electrostatic attraction between the Li^{1+} ion and the six surrounding O^{2-} ions making it more difficult to remove the lithium from the 6c site.

4.6. Tritium solubility at lithium sites

Given the likely high concentration of lithium vacancy defects as the material ages it is anticipated that this defect will play an important role in the accommodation and diffusion[45] of tritium in the crystal. Therefore, we now examine substitution of tritium onto the lithium sublattice, (i.e. T_{Li}^{0}). Previous DFT studies of tritium accommodation in Li_2TiO_3 show that the tritium will move from the Li site and bond with a nearest neighbour oxygen atom to form a hydroxide that could be considered to be a $\{V_{Li}^{1-} : T_i^{1+}\}$ cluster[16]. Li *et al.* have shown that the energy of the resulting hydroxide bond depends on exactly which of the nearest neighbour oxygens the tritium ion bonds to[18]. Therefore, here we investigate the energy for all possible hydroxide orientations around both Li vacancies in Li_8PbO_6 and the results are presented in table 4.

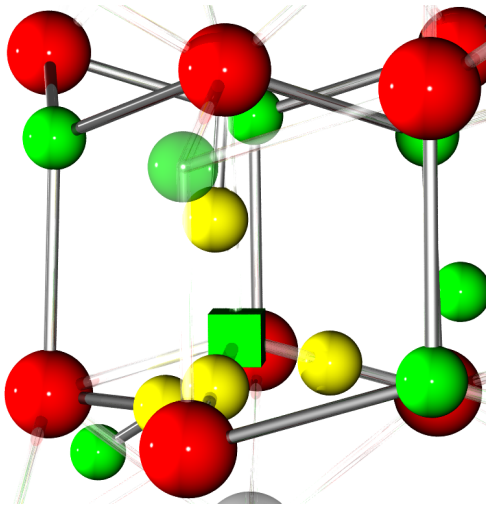

Figure 10: Possible tritium sites for $\{V_{Li}^{1-} : T_i^{1+}\}$ defect clusters at the Li1 site. Grey, green and red spheres represent the lead, lithium and oxygen ions respectively. Yellow spheres represent the possible tritium sites and the green cube represents a lithium vacancy site.

The data presented in table 4 shows that there are four symmetrically distinct $\{V_{Li}^{1-} : T_i^{1+}\}$ clusters involving the tetrahedral Li1 site. By contrast, despite there being six oxygen nearest neighbours surrounding the Li2 site, there appear to be just two symmetrically distinct hydroxides formed in both VASP and CASTEP models due to the symmetry of the crystal. Once again, like the lithium vacancy defects there is excellent agreement in formation energies produced by both codes, with a

Table 4: Defect formation energies for the tritium accommodation at lithium vacancy defects in Li_8PbO_6. Also included are the resulting O-H bond distances

		CASTEP		VASP	
Lithium site	O atom	E_f /eV	r(O − H) /Å	E_f /eV	r(O − H) /Å
Li1	1	1.591	0.988	1.593	0.989
(18f)	2	1.437	0.980	1.438	0.980
	3	1.491	0.986	1.490	0.990
	4	1.747	0.990	1.747	0.991
Li2	1	1.769	0.982	1.783	0.984
(6c)	2	1.769	0.982	1.785	0.983
	3	1.769	0.982	1.784	0.986
	4	1.880	0.985	1.892	0.988
	5	1.880	0.985	1.891	0.986
	6	1.880	0.985	1.889	0.987

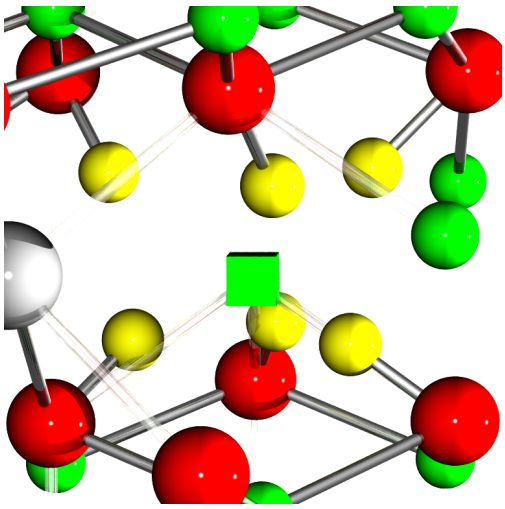

Figure 11: Possible tritium sites for $\{V_{\mathrm{Li}}^{1-} : T_i^{1+}\}$ defect clusters at the Li2 site.

discrepancy of less than 20 meV. Visualisations of the $\{V_{\mathrm{Li}}^{1-} : T_i^{1+}\}$ defect clusters are given in figures 10 and 11.

The formation energies for the $\{V_{\mathrm{Li}}^{1-} : T_i^{1+}\}$ indicate that tritium will preferentially form a hydroxide that is bound to an Li1 site.

5. Conclusion

Thermal, elastic and electronic properties of Li_8PbO_6 have been examined via first principles simulations using DFT. Formation energies for lithium vacancy defects and $\{V_{\mathrm{Li}}^{1-} : T_i^{1+}\}$ defect clusters have been determined. Despite the different basis sets used, there is a remarkable level of agreement between codes for many of the fundamental properties properties of Li_8PbO_6. This is especially true for defect formation energy calculations, which are accurate to within 0.1 eV of each other. We were able to show there is a preference in Li_8PbO_6 for lithium vacancies to form at 18f Wyckoff sites and consequentially we expect more native vacancies to form here rather than at 6c sites. We have also shown there is a preference for tritium to bond to nearest neighbour oxygen sites at lithium 18f sites over 6c sites, suggesting higher accomodation of tritium at the 18f sites in general.

6. Acknowledgements

This work was conducted using the High End Computing facility at Lancaster University. Simulations were performed using the ARCHER UK National Supercomputing Service (http://www.archer.ac.uk) via our membership of the UK's HEC Materials Chemistry Consortium, which is funded by EPSRC (EP/L000202, EP/R029431). We would like to offer our personal thanks to Robert Woodman and Tokamak Energy for their support, without whom this publication (and other future works on Li_8PbO_6 conducted by us) would not have been possible. This work was also supported by the ESPRC-funded Centre for Doctoral Training in GREEN (Growing skills for Reliable Economic Energy from Nuclear) (Grant code: EP/S022295/1).

References

[1] R. M. Brown, W. E. Grummitt, The determination of tritium in natural waters, Can. J. Chem. 105 (4) (1956) 220–226.

[2] L. Giancarli, M. Abdou, D. Campbell, V. Chuyanov, M. Ahn, M. Enoeda, C. Pan, Y. Poitevin, E. Raendra Kumar, I. Ricapito, Y. Strebkov, S. Suzuki, P. Wong, M. Zmitko, Overview of the ITER TBM program, Fus. Eng. Des. 87 (2012) 395–402.

[3] W. E. Lee, M. Gilbert, S. T. Murphy, R. W. Grimes, Opportunities for advanced ceramics and composites in the nuclear sector, J. Amer. Ceram. Soc. 96[7] (2013) 2005–2030.

[4] M. Abdou, N. B. Morley, S. Smolentsev, A. Ying, S. Malang, A. Rowliffe, M. Ulrickson, Blanket/first wall challenges and required R&D on the pathway to DEMO, Fus. Eng. Des. (2015) 2–43.

[5] S. J. Piet, D. W. Jeppson, L. D. Muhlestein, M. S. Kazimi, M. L. Corradini, Liquid metal chemical reaction safety in fusion facilities, Fus. Eng. Des. 5 (1983) 273–298.

[6] T. Ihli, T. K. Basu, L. M. Giancarli, S. Konishi, S. Malang, F. Najmabadi, S. Nishio, A. R. Raffray, C. V. S. Rao, A. Sagara, Y. Wu, Review of blanket designs for advanced fusion reactors, Fus. Eng. Des. 83 (2008) 912–919.

[7] M. H. H. Kolb, K. Mukai, R. Knitter, T. Hosino, Li_4SiO_4 based breeder ceramics with Li_2TiO_3, $LiAlO_2$ and $Li_xLa_yTiO_3$ additions, part i: Fabrication, Fus. Eng. Des. 115 (2017) 39–48.

[8] M. Xiang, Y. Zhang, Y. Zhang, S. Liu, H. Liu, C. Wang, C. Gu, Preparation of Li_2TiO_3-Li_4SiO_4 core-shell ceramic pebbles with enhanced crush load by graphite bed process, J. Nucl. Mater. 466 (2015) 477–483.

[9] R. Chen, M. Yang, Y. Shi, H. Wang, H. Guo, Y. Zeng, J. Qi, Q. Shi, Z. Liao, T. Lu, Development of an advanced core-shell ceramic pebble with Li_4TiO_4 pure phase core and Li_2TiO_3 nanostructured shell by a physical coating method, J. Nucl. Mater. 520 (2019) 252–257.

[10] M. L. Jackson, P. A. Burr, R. W. Grimes, Defect processes in Be_{12}x (x=Ti,Mo,V,W), Nucl. Fus. 57 (2017) 086049.

[11] F. A. Hernandez, P. Pereslavtsev, First principles review of options for tritium breeder and neutron multiplier materials for breeding blankets in fusion reactors, Fus. Eng. Des. 137 (2018) 243–256.

[12] T. Hayashi, S. Konishi, K. Okuno, Tritium release behavior from neutron-irradiated Li_8PbO_6, J. Nucl. Mater. 170 (1990) 60–65.

[13] I. Palermo, J. M. Gómez-Ros, G. Veredas, L. Sedano, J. P. Catalán, F. Ogando, J. S. Recio, Preliminary neutronic assessment of a helium-cooled Li_8PbO_6 breeding blanket design for DEMO, Fus. Eng. Des. 87 (2012) 195–199.

[14] S. T. Murphy, P. Zeller, A. Chartier, L. Van Brutzel, Atomistic simulation of the structural, thermodynamic and elastic properties of Li_2TiO_3, J. Phys. Chem. C 115 (2011) 21874–21881.

[15] T. Tang, D.-L. Luo, Density functional theory study of electronic structures 3 in lithium silicates: Li_2SiO_3 and Li_4SiO_4, J. At. Mol. Sci. 1 (3) (2010) 185–200.

[16] S. T. Murphy, Tritium solubility in Li_2TiO_3 from first principles simulations, J. Phys. Chem. C 118 (2014) 29525–29532.

[17] Y. Shi, T. Lu, T. Gao, X. Xiang, Q. Zhang, X. Yu, Y. Gong, M. Yang, Density functional study of lithium vacancy in Li_4SiO_4: Trapping of tritium and helium, J. Nucl. Mater. 467 (2015) 519–526.

[18] K. Li, W.-H. Wang, Y. T. Li, First principles study of tritium diffusion in Li_2TiO_3 crystal with lithium vacancy, Mater. (Basel) 11 (2018) 2383.

[19] G. Kresse, J. Furthmüller, Efficient iterative schemes for ab initio total-energy calculations using a plane-wave basis set, Phys. Rev. B 54 (1996) 11169.

[20] M. D. Segall, P. J. D. Lindan, M. J. Probert, C. J. Pickard, P. J. Hasnip, S. J. Clark, M. C. Payne, First-principles simulation: ideas, illustrations and the CASTEP code, J. Phys.: Condens. Matter 14 (2002) 2717–2744.

[21] S. Clark, M. Segall, C. Pickard, P. Hasnip, K. Refson, M. Payne, First principles methods using CASTEP, Z. Kristallogr. 220 (2005) 567–570.

[22] J. P. Perdew, K. Burke, M. Ernzerhof, Generalized gradient approximation made simple, Phys. Rev. Lett. 77(18) (1996) 3868.

[23] J. Heyd, G. E. Scuseria, M. Ernzerhof, Hybrid functionals based on a screened coulomb potential, J. Chem. Phys. 118 (2003) 8207.

[24] H. J. Monkhorst, J. D. Pack, Special points for brillouin-zone integrations, Phys. Rev. B 13 (1976) 5188.

[25] G. Kresse, D. Joubert, From ultrasoft pseudopotentials to the projector augmented-wave method, Phys. Rev. B 59 (1999) 1758.

[26] B. Barzel, R. Hoppe, Zur kristallstruktur von Li_8PbO_6, Z. Anorg. Allg. Chem 515 (1984) 81–86.

[27] S. Hull, T. W. D. Farley, W. Hayes, M. T. Hutchings, The elastic properties of lithium oxide and their variation with temperature, J. Nucl. Mater. 160 (1988) 125–134.

[28] J. E. Taggart, E. E. Foord, A. Rosenzweig, T. Hanson, Scrutinyite, natural occurrences of αPbO_2 from bingham, new mexico, u.s.a., and mapimi, mexico, Can. Miner. 26 (1988) 905–910.

[29] E. J. Convington, D. J. Montgomery, Lattice constants of separated lithium isotopes, J. Chem. Phys. 27 (1957) 1030–1032.

[30] H. P. Klug, A redetermination of the lattice constant of lead, J. Am. Chem. Soc. 68 (1946) 1493–1494.

[31] K. P. Huber, G. Herzberg, Molecular Spectra and Molecular Structure, Springer, 1979.

[32] S. B. Zhang, J. E. Northup, Chemical potential dependence of defect formation energies in GaAs: Application to Ga self-diffusion, Phys. Rev. Lett. 67 (1991) 2339–2242.

[33] S. T. Murphy, N. D. M. Hine, Anisotropic charge screening and supercell size convergence of defect formation energies, Phys. Rev. B 87 (2013) 094111.

[34] T. R. Durrant, S. T. Murphy, M. B. Watkins, A. L. Shluger, Relation between image charge and potential alignment corrections for charged defects in periodic boundary conditions, J. Chem. Phys. 149 (2018) 024103.

[35] M. Gajdoš, K. Hummer, G. Kresse, J. Furthmüller, F. Bechstedt, Linear optical properties in the projector-augmented wave methodology, Phys. Rev. B 73 (2006) 045112.

[36] S. Baroni, S. de Gironcoli, A. D. Corso, P. Gianozzi, Phonons and related crystal properties from density-functional perturbation theory, Rev. Mod. Phys. 73 (2001) 515.

[37] A. Togo, I. Tanaka, First principles phonon calculations in materials science, Scr. Mater. 108 (2015) 1–5.

[38] K. Refson, S. J. Clark, P. R. Tulip, Variational density functional perturbation theory for dielectrics and lattice dynamics, Phys. Rev. B 73 (2006) 155114.

[39] M. W. Chase Jr., C. A. Davies, J. R. Downey, D. J. Frurip, R. A. McDonald, A. N. Syverud, NIST JANAF thermochemical tables 1985, NIST, 1986.

[40] Z. Wan, Y. Yu, H. F. Zhang, T. Gao, X. J. Chen, C. J. Xiao, First-principles study of electronic, dynamical and thermodynamic properties of Li_2TiO_3, Eur. Phys. J. B 85 (2012) 181.

[41] J. Yan, T. Gao, S. Ma, X. Chen, C. Xiao, T. Lu, First-principles calculation of the structural, electronic, dynamical, and thermodynamic properties of Li_4TiO_4, Fus. Eng. Des. 129 (2018) 241–246.

[42] S. Ma, Y. Shen, X. Kong, T. Gao, X. Chen, C. Xiao, T. Lu, A new interatomic pair potential for the modeling of crystalline Li_2SiO_3, Mater. Des 118 (2017) 218–225.

[43] S. Colominas, I. Palermo, J. Abella, J. M. Gómez-Ros, J.

Sanz, L. Sedano, Octalithium plumbate as a breeding blanket ceramic: Neutronic performances, synthesis and partial characterization, Fus. Eng. Des. 87 (2012) 482–485

[44] X. Xiang, W. Zhu, T. Lu, T. Gao, Y. Shi, M. Yang, Y. Gong, X. Yu, L. Feng, Y. Wei, Z. Lu, Density functional theory calculations of point defects and hydrogen isotopes in Li_4SiO_4, AIP Adv. 5 (2015) 107136.

[45] K. N. Goswami, S. T. Murphy, Influence of lithium vacancy defects on tritium diffusion in β-Li_2TiO_3, J. Phys. Chem. C 124 (23) (2020) 12286–12294.